Multimaterial 3-D-Printed FSSs for Ultrawide and Dual Passbands in the K–Ka Spectra

Xiaojing Lv, *Member, IEEE*, Yang Yang, *Senior Member, IEEE*, Zhen Luo, and J. Scott Tyo, *Fellow, IEEE*

***Abstract*— This article presents two 3-D bandpass frequency-selective surfaces (FSSs) featuring ultrawide and dual operating frequency spectra, respectively. Leveraging advanced multimaterial additive manufacturing, the design potential of 3-D meta-atoms can be unlocked. Compared to conventional 2.5-D or quasi-3-D FSSs that incorporate vias or microstrip lines, the proposed centrally loaded geometries facilitate in-depth topological optimization. The assembly of diverse fundamental FSS shapes introduces multiple poles and zeros, contributing to broad in-band transmission, extensive out-of-band rejections, and sharp transitions while still attaining simplicity when using equivalent circuit–transmission line modeling and associated qualitative design aids. The application-oriented FSSs are properly configured to fit the K–Ka spectra, where the ultrawideband FSS covers a fractional bandwidth of approximately 2:1, and the dual-band FSS offers two near-equal absolute bandwidths of 8 GHz. Both designs are inherently polarization insensitive due to unit-cell symmetry, and their robustness against oblique incidences has also been experimentally verified for both TE and TM modes.**

***Index Terms*— Dual-band, frequency-selective surface (FSS), meta-atom, multimaterial additive manufacturing, out-of-band rejection, 3-D printing, ultrawideband.**

I. Introduction

FREQUENCY-SELECTIVE surface (FSS) is typically a planar structure exhibiting 2-D periodicity [2], [3], [4]. Analogous to employing a conductive solenoid as an electromagnet, intrinsic material attributes can be emulated and approached by optimizing the geometric topology of unit cells, also referred to as meta-atoms [4]. To ensure equivalent in-plane homogeneity and therefore avoid the occurrence of higher-order modes, the unit-cell dimensions must conform to the subwavelength criterion [3]. FSS-based spatial filters prioritize their inherent frequency-selective characteristics, establishing a basis for extended applications across diverse scenarios, such as radar domes [5], [6], [7], electromagnetic (EM) absorbers [8], [9], [10], [11], transmissive arrays [12], [13], [14], and Fabry–Pérot (FP) antennas [15], [16], [17], [18].

A prototypical unit cell is assembled by alternately layering 2-D metallic patterns with dielectric spacers. Without increasing the number of layers or thickness profiles, the planar patterns become progressively more intricate for merely diminishing marginal enhancement in performance. Additional geometric features, however, do not always warrant improved performance, as exemplified by the semi-analytical design method proposed for FSS-based absorbers [9]. Along the EM wave propagation path, the nonmagnetic dielectric layers can be characterized solely by thicknesses and permittivities, reserving high degrees of freedom (DoFs) for integrating metallic waveguiding structures. The 2.5-D FSS designs employ vertical vias to enhance capabilities in manipulating capacitive couplings and self-inductance [19], [20], [21]; nevertheless, the third dimension remains underutilized. Alternatively, identical microstrip lines can be incorporated on a pair of opposite unit-cell boundaries [22], [23]. Compared to linear vias, this configuration offers enhanced topological versatility, facilitating exceptional specifications in spatial filter design, such as broad bandwidth, sharp transitions, extensive out-of-band rejections, and high angular stability, albeit only in one polarization direction. With a substantial tradeoff in filtering performance, polarization insensitivity can be obtained by incorporating identical microstrip line insertions on all unit-cell boundaries [24], [25], rendering this prototype indistinguishable from a conventional square waveguide (SW) array [26], [27]. The topological optimization of a generalized SW unit cell remains confined to the boundary planes, without fully leveraging the free space within the 3-D lattice. The quasi-3-D FSS-based filters, implemented with via or microstrip line configurations, also present miniaturization challenges with the readily available manufacturing techniques; consequently, the operational frequencies of the state-of-the-art designs are capped up to the Ku-band [19], [20], [21], [22], [23], [24], [25], [26], [27].

Advanced multimaterial additive manufacturing lifts the constraints of spatial modeling [28], thereby unlocking the full design potential of 3-D meta-atoms. Facilitated by topological optimization, this printing technology also enables the miniaturization and integration of meta-atoms, which

Received 30 June 2024; revised 2 October 2024; accepted 3 November 2024. Date of publication 25 November 2024; date of current version 7 January 2025. This work was supported in part by the Australian Office of National Intelligence–National Intelligence and Security Discovery Research Grant Program under Grant NI220100074, in part by the Australian Research Council–ARC Linkage Projects under Grant LP210300004 and Grant LP230200030. This article is an extended version of a conference paper presented at the IEEE MTT-S 2024 International Microwave Symposium (IMS) in Washington, DC, USA [DOI: 10.1109/IMS40175.2024.10600453]. *(Corresponding authors: Yang Yang; Zhen Luo.)*

Xiaojing Lv and Zhen Luo are with the School of Mechanical and Mechatronic Engineering, University of Technology Sydney, Ultimo, NSW 2007, Australia (e-mail: xiaojing.lv@uts.edu.au; zhen.luo@uts.edu.au).

Yang Yang is with the School of Electrical and Data Engineering, University of Technology Sydney, Ultimo, NSW 2007, Australia (e-mail: yang.yang.au@ieee.org).

J. Scott Tyo is with the Department of Electrical and Computer Systems Engineering, Monash University, Clayton, VIC 3800, Australia (e-mail: scott.tyo@monash.edu).

Color versions of one or more figures in this article are available at https://doi.org/10.1109/TMTT.2024.3497996.

Digital Object Identifier 10.1109/TMTT.2024.3497996

© 2024 The Authors. This work is licensed under a Creative Commons Attribution 4.0 License.
For more information, see https://creativecommons.org/licenses/by/4.0/

accommodates higher operating frequencies for 5G and future telecommunications. The additively manufactured electronics (AME) enable seamless prototyping of 3-D metallic structures in a single substrate with high resolution and accurate positioning of traces, which justifies the requirement for fabricating compact and ultrathin 3-D-FSS-based designs [28], [29]. To optimize a meta-atom leveraging practically accessible computing power, implementing effective and efficient design methods is imperative. The equivalent circuit–transmission line modeling exhibits physical insights into planar metallic shapes (i.e., circuit branches) and homogeneous dielectric layers (i.e., transmission lines); however, its applicability to metallic parts spanning in the EM wave propagation direction requires further exploration, and the complexity significantly escalates when analyzing nonfundamental geometries.

This article elucidates the benefits of adopting 3-D prototyping and additive manufacturing for enhanced frequency-selective performance, which is exemplified through the most emblematic application: bandpass filtering. The potential of centrally loaded 3-D unit-cell geometries has been exploited for ultrawide and dual-band spatial filtering that is highly sought after in wireless communication applications. These proposed designs are assembled from various fundamental FSS shapes, such as patches, strips, loops, and grids, which ensures the simplicity of the equivalent circuit branches whilst affording sufficient DoFs to fully optimize the meta-atoms. Within the equivalent circuit–transmission line modeling framework, structures aligned with the EM wave propagation direction are represented as successive sections of effective media. Its reliability has been corroborated by comparing the S-parameters obtained from circuit calculations and full-wave simulations. The Smith Chart, as an intuitive tool for qualitative analysis, has also been employed to monitor the real-time variations of the input admittance locus during topological optimization. The finalized designs operate in the K- and Ka-bands, featuring efficient in-band transmissions, clear out-of-band rejections, polarization insensitivity, and robustness at oblique incident angles for both TE and TM modes. The ultrawide bandpass filter covers a -3-dB bandwidth from 18.23 to 37.49 GHz, while the dual-band design offers two near-equal operating frequency ranges spanning 17.21 to 25.29 GHz and 29.62 to 37.45 GHz, respectively. The ultrawide and dual-band FSSs have been fabricated by the additive manufacturing platform DragonFly[1] IV and subsequently experimentally verified for transmissivity and reflectivity.

II. 3-D Centrally Loaded Meta-Atoms for Ultrawide Passband

The square ring resonator exhibits a narrowband bandstop frequency response among the collection of fundamental 2-D-FSS shapes [2]. Its complementary geometry, namely a square mesh with a centrally loaded patch, operates as a bandpass filter of the same bandwidth following Babinet's Principle. A wider passband and steeper roll-off skirts can be achieved by stacking a pair of identical FSSs at a certain distance apart. In principle, its performance can be further

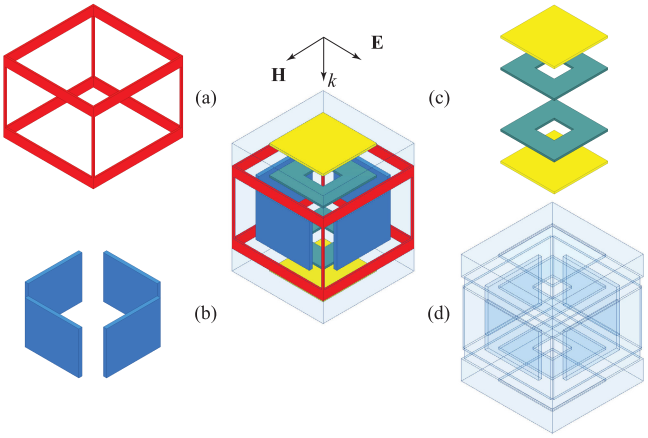

Fig. 1. Exploded view and assembly of the 3-D meta-atom evolved based on a 2-D centrally loaded prototype. (a)–(c) Conductive structures, including a hexahedral grid frame (red), side enclosures (blue), and a stack of square patches (yellow) and square rings (cyan), respectively. (d) Supporting dielectric.

enhanced by incorporating geometric features into the FSS layers, which introduces more transmission poles and zeros. However, the corresponding modeling of 2-D patterns for equivalent circuit branches also becomes more sophisticated and the mutual couplings between lumped inductive or capacitive elements are nonnegligible. Instead, metallic structures can be integrated along the EM wave propagation path to fully exhaust the design potential of a 3-D meta-atom.

A 3-D unit-cell geometry evolved from the 2-D centrally loaded prototype is shown in Fig. 1, where different colors are adopted only for the visual distinction of geometric features. The quadrilateral mesh is transformed into a hexahedral grid, with square patches affixed onto the central axis of each cubic lattice face. A pair of square ring resonators has also been incorporated to create additional transmission poles within the ultrawide operating frequency range. The conductive geometries along the direction of EM wave propagation, including the supporting pillars of the grid frame (red) and the side enclosures (blue), effectively function as an integrated waveguiding structure, which plays a vital role in wideband impedance matching with free space. Insensitivity to polarization is realized by the inherent symmetry of the meta-atom. Parametric configurations are provided in the caption of Fig. 2. For simplicity in manufacturing and to accommodate fabrication tolerances, the layer thicknesses and wall widths of the conductive structures have been standardized to th $=$ 50 μm and $w = 100$ μm, respectively. The permittivity ϵ_d of the dielectric substrate is set at 2.78 in consistent with the available acrylate ink for the DragonFly IV printer.

The 3-D meta-atom lattice is periodically extended using primary and secondary boundary conditions and excited by Floquet ports in the Ansys High-Frequency Structure Simulator (HFSS[2]). The full-wave simulated ideal S-parameters, assuming the dielectric substrate is lossless (i.e., $\tan\delta = 0$) and all the metallic parts are composed of pure and unoxidized silver, are presented in Fig. 3(a). Targeting a reflectivity of -10 dB, the passband spans from 18.7 to 40 GHz, which

[1]Registered trademark.

[2]Trademarked.

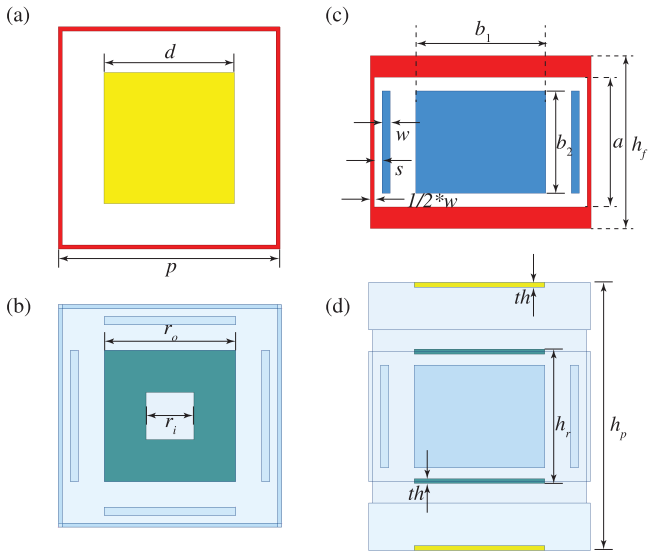

Fig. 2. Parametric configurations for the 3-D meta-atom in Fig. 1. (a) and (b) Top views that illustrate the square patch, the square ring, and the unit-cell periodicity. (c) and (d) Side views that illustrate the grid frame, the side enclosures, and the vertical spacings of the layers. Specifically, the dimensional parameters are $p = 2.8$ mm, $d = 1.65$ mm, $s = 0.15$ mm, $r_o = 1.65$ mm, $r_i = 0.6$ mm, $a = 1.65$ mm, $b_1 = 1.65$ mm, $b_2 = 1.3$ mm, $h_r = 1.7$ mm, $h_f = 2.2$ mm, and $h_p = 3.4$ mm.

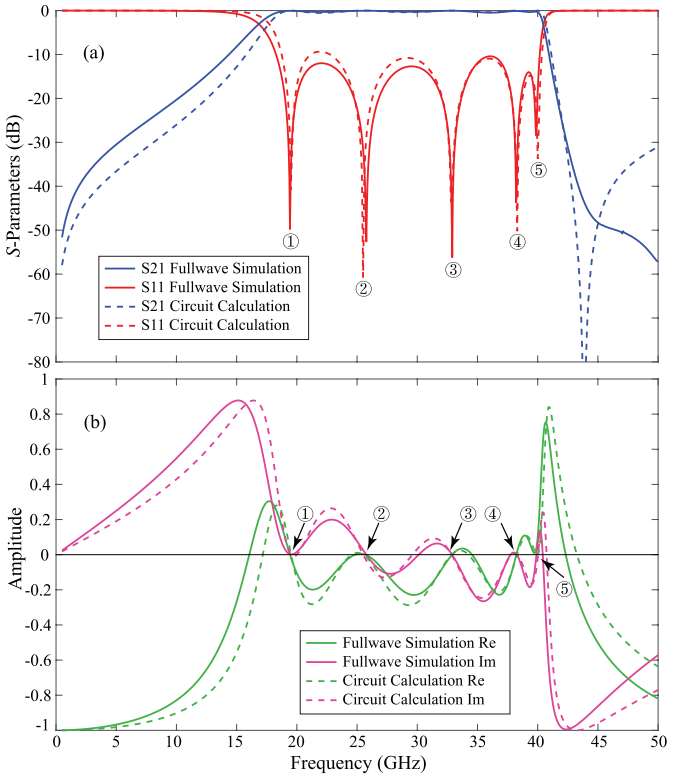

Fig. 3. Full-wave simulated and circuit-calculated transmission and reflection coefficients. (a) S-parameters in dB scale. (b) Real (green) and imaginary (magenta) parts for reflection coefficients. Transmission poles are indicated with circled numbers.

nearly perfectly encompasses the K–Ka spectra. Five transmission poles are distributed across the operating frequency range, while the higher transition exhibits a steep roll-off skirt followed by extensive out-of-band rejection. Though equivalent circuit–transmission line modeling readily provides physical insights into the working mechanisms of 2-D-FSS-based

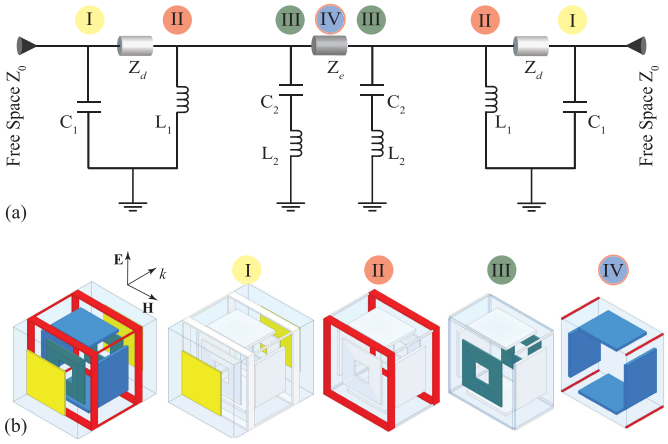

Fig. 4. Equivalent circuit–transmission line modeling for the 3-D meta-atom. (a) Characteristic impedance of free space $Z_0 = 377\ \Omega$. The lumped circuit elements $C_1 = 24.40$ fF, $C_2 = 23.90$ fF, $L_1 = 464.12$ pH, and $L_2 = 550.96$ pH. (b) Each equivalent circuit branch or transmission line section is modeled based on distinct geometric topology as highlighted from I to IV along the wave propagation path. The electrical lengths of transmission lines are approximately $\Theta_d = 34°$ and $\Theta_e = 165°$ when referenced at 30 GHz.

designs, the authors aim to further underscore its versatility in analyzing this 3-D multiresonance meta-atom. As illustrated in Fig. 4, each lumped circuit branch or transmission line section in (a) corresponds to a specific geometric feature from I to IV in (b), which facilitates the synthesis and optimization of the topological structure. In essence, gaps perpendicular to the electric field are represented as capacitors, metallic strips aligned with the electric field are depicted as inductors, and the dielectric layers are described as transmission lines characterized by permittivity and electrical length. In Fig. 4(a), the capacitor C_1 corresponds to the square patch, the inductor L_1 corresponds to the square grid, the capacitor C_2 and inductor L_2 in series corresponds to the square ring, and the effective transmission line characterized by the intrinsic impedance Z_e and electrical length Θ_e represents the central waveguiding structure. The simplicity of this equivalent circuit–transmission line model stems from integrating independent fundamental FSS shapes in the meta-atom and employing effective medium equivalent ($\epsilon_e = 9.13$) for its intricately structured waveguiding part IV. The intrinsic impedance for nonmagnetic natural or effective dielectric material (e.g., Z_d or Z_e) can be calculated as

$$Z = \sqrt{\frac{\mu}{\epsilon}} = \sqrt{\frac{\mu_0}{\epsilon_0 \epsilon_r}} = \frac{Z_0}{\sqrt{\epsilon_r}} \tag{1}$$

where ϵ_r is the relative permittivity. The frequency-dependent electrical length (e.g., Θ_d or Θ_e) can be expressed in degrees

$$\Theta = \frac{h}{\lambda_o}\sqrt{\epsilon_r} \times 360° = \frac{h}{c/f_o}\sqrt{\epsilon_r} \times 360° \tag{2}$$

where h is the absolute length, c is the speed of light, and f_o is the reference frequency. As listed in the caption of Fig. 4, the lumped circuit elements can be configured using empirical formulas derived from the semi-analytical algorithm [9]. The circuit-calculated transmission and reflection coefficients closely align with the full-wave simulated results, as shown in Fig. 3(a), especially at all the transmission poles within the working frequency range. The mismatch at approximately

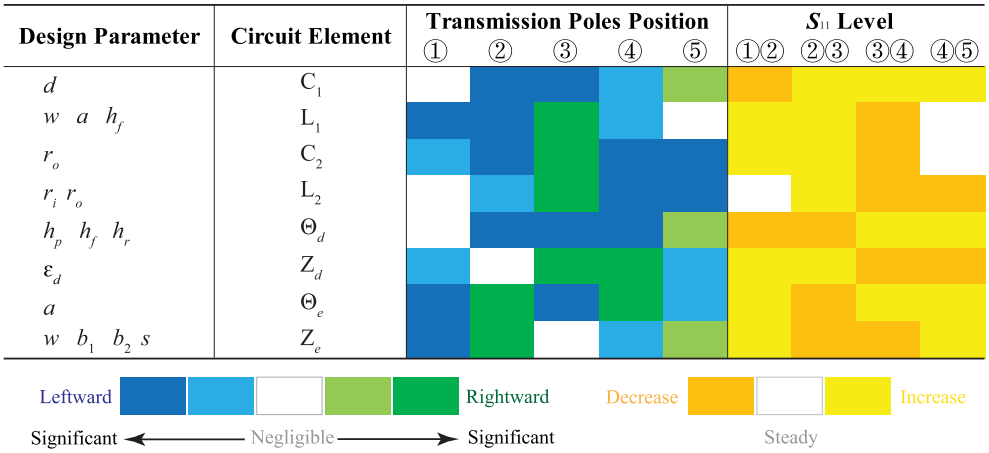

Fig. 5. Qualitative synthesis aid that interconnects the design parameters, equivalent circuit elements, and frequency response performance. The directions and extents of pole shift caused by the increment of each circuit–transmission line element are visualized in shades of navy blue (significantly leftward), light blue (slightly leftward), white (steady), mint green (slightly rightward), and dark green (significantly rightward), while the changes in the level of reflectivity between adjacent poles are represented by yellow (increase), white (steady), and orange (decrease), respectively.

−40 dB in the upper stopband of the ultrawide frequency range is a result of the tradeoff between achieving extreme accuracy and maintaining analytical simplicity when modeling the equivalent circuit–transmission line. Beyond the amplitude in dB scale, the real and imaginary parts of the complex reflection coefficients from both full-wave simulation and circuit calculation also have been compared to further validate the reliability of the design approach, as illustrated in Fig. 3(b), where transmission poles are indicated by the simultaneous zero crossing of the real and imaginary parts. The real and imaginary components are equivalent to the magnitude and phase representation, which are critical when adopting the 3-D meta-atom lattices to construct metasurfaces, such as transmitarrays. Intricate, yet subtle mutual couplings are inevitable even in multilayer 2-D-FSSs, and the values for equivalent lumped elements cannot maintain absolute constancy across an ultrawide frequency spectrum, due to nonnegligible changes in wavelength. Striking a balanced tradeoff between an explicitly detailed circuit–transmission line model and computational efficiency is one of the primary design principles.

The full-wave parametric study demands substantial computational resources and time, yet it lacks in-depth physical insights for facilitating the topological optimization of established geometric shapes. The equivalent circuit–transmission line model is, however, widely utilized for analyzing rather than the synthesis of designs in the literature. To bridge the gaps in-between the dimensional parameters of a 3-D meta-atom, the lumped elements of its equivalent model, and the frequency response performance, a qualitative design approach has been developed, as illustrated in Fig. 5. The first two columns reflect the mapping between the dimensional parameters and material attributes of the 3-D lattice, and the equivalent elements in the circuit–transmission line model. In the last two columns, different color modules intuitively and informatively delineate changes in the reflection coefficient as the values of the corresponding equivalent elements increase, from the perspective of pole positions along the frequency axis and levels of reflectivity along the amplitude axis. A desired frequency response in the specified operating spectrum can be approximated by a comprehensive and weighted amalgamation of color schemes that are aligned with the mapping from equivalent circuit elements to 3-D meta-atom dimensions or material attributes. This design tool can be seamlessly implemented into the topological optimization of other FSS-based structures, where the tabulated color modules can be efficiently obtained via the tuning interface in the advanced design system (ADS[2]). The poles within the passband are determined by resonances: electrical resonance generated by capacitors and inductors, or cavity resonance caused by constructive and destructive wave interference at different positions. In the proposed 3-D meta-atoms, the frequency of each pole reflects the combined effect of multiple equivalent components.

The Smith Chart is an intuitive design tool for simultaneously assessing the impedance matching across the fractional intervals between transmission poles when configuring specific geometric dimensions or integrating new topological geometries, as referenced in Fig. 5. The aimed level of reflectivity (e.g., −10 dB) can be represented by the standing wave ratio (SWR) circle, with the segment of the admittance locus that falls inside it indicating effective impedance matching, as illustrated in Fig. 6. Considering the asymmetric and nonlinear characteristics of the Smith Chart, broadband impedance matching can be achieved by incorporating geometric features along the EM wave propagation path to cluster the locus into a predetermined SWR circle, which is exactly the motivation for proposing and developing 3-D meta-atoms. More specifically, by adding a dielectric spacer as a transmission line section in conjunction with placing a resonating geometry as a shunt circuit branch atop the existing structure, the input admittance becomes

$$Y_{\text{in}} = Y_e \frac{Y_{\text{ex}} + jY_e \tan \beta h}{Y_e + jY_{\text{ex}} \tan \beta h} + Y_{\text{add}} \tag{3}$$

where Y_{ex} is the existing input admittance, Y_e is the intrinsic admittance for nonmagnetic natural or effective dielectric material, Y_{add} is the admittance introduced by the incorporated geometry, and $\beta = 2\pi f(\epsilon_e \epsilon_0 \mu_0)^{1/2}$ is the propagation constant. As a supplement to Figs. 3 and 5, transmission poles can also be simultaneously monitored by tracking the admittance locus passing through the center of the Smith Chart, while

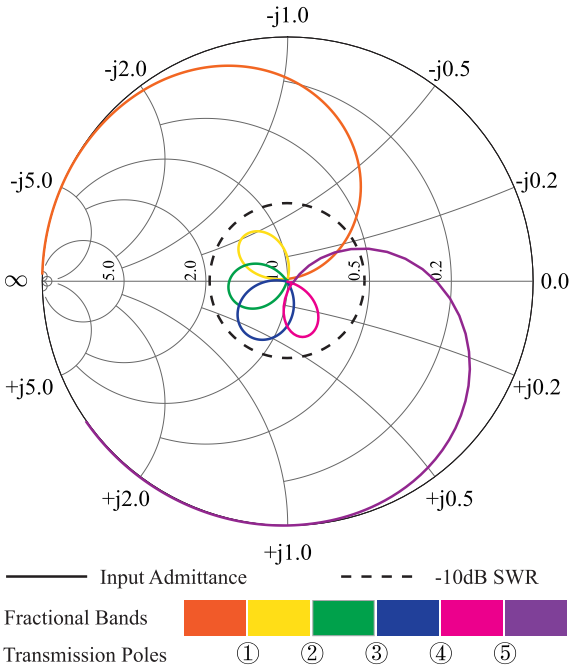

Fig. 6. Admittance Smith Chart. The locus clustered within the −10-dB SWR dash circle corresponds to the ultrawide passband ranging from 18.7 to 40 GHz. The five transmission poles can be individually identified whenever the trace passes through the center, and the fractional bands are highlighted with different colors.

the level of reflectivity between adjacent poles can be inferred from the curvature and the area of each knot-like loop.

III. Revised Meta-Atoms With Additional Transmission Zeros

A. Ultrawide Bandpass FSS With Bilateral Sharp Transitions

The frequency response of the ultrawide bandpass filter described in Section II excels across comprehensive evaluation criteria, including an ultrawide passband covering K–Ka spectra, less than 1-dB insertion loss and at least 30-dB stopband attenuation. The higher end of the operating frequency spectrum exhibits a steep roll-off skirt, whereas the transition at the lower end is not sufficiently sharp due to the absence of transmission zeros. This section demonstrates how additional transmission zeros can be introduced to sharpen the lower-end transition and further widen its out-of-band rejection without significantly redesigning the existing 3-D meta-atom. The design technique is widely applicable and can be adopted to overhaul a broad range of FSSs or meta-materials.

To introduce transmission zeros below the lowest operating frequency (i.e., at longer wavelengths), the incorporated geometric shape needs to be larger than the existing metallic resonators in the meta-atom. As shown in Fig. 7(a), and in comparison to Fig. 1, slits are introduced between the adjacent hexahedral grids (red). Additional rectangular plates (orange) are also integrated to vertically enclose the center, mitigating the deterioration of in-band transmission and disruption of working bandwidth caused by the slits. The retained geometric features, as first referenced in Fig. 2, are slightly reconfigured to optimize the frequency response, where $w_1 = 100\ \mu m$, $w_2 = 75\ \mu m$, $p = 3.1$ mm, $d = 1.8$ mm, $s = 0.125$ mm,

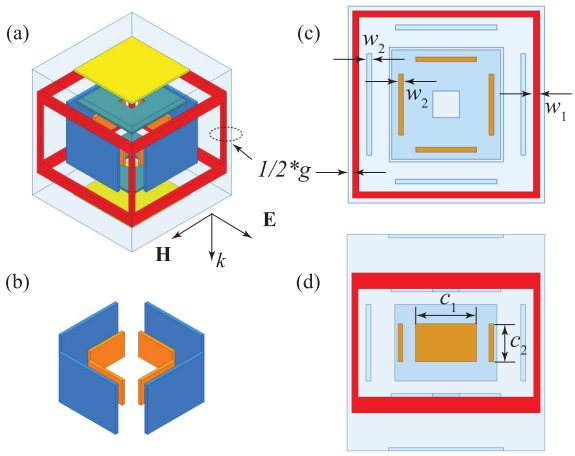

Fig. 7. Revised 3-D meta-atom for ultrawide bandpass filtering with bilateral sharp transitions. (a) Assembled unit-cell geometry. (b) Added central loading (orange) for stabilizing the in-band transmission level and retaining operating bandwidth. (c) and (d) Top and side views that illustrate the dimensions of the new geometric features. Specifically, the dimensional parameters are $g = 0.15$ mm, $c_1 = 0.96$ mm, and $c_2 = 0.6$ mm.

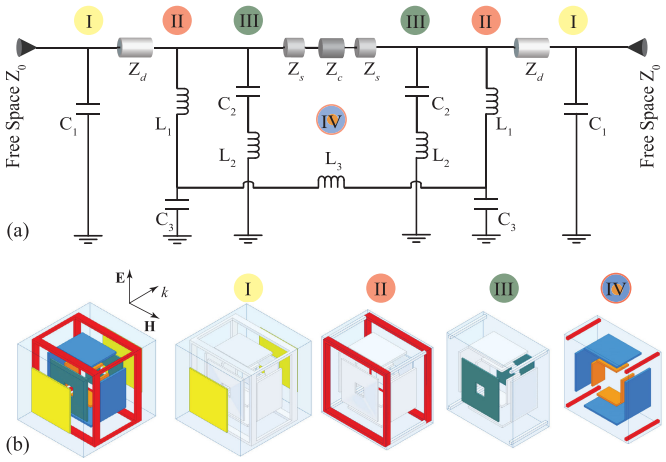

Fig. 8. Equivalent circuit–transmission line modeling for the revised 3-D meta-atom. (a) Lumped circuit elements $C_1 = 25.56$ fF, $C_2 = 31.88$ fF, $C_3 = 916.15$ fF, $L_1 = 484.87$ pH, $L_2 = 449.30$ pH, and $L_3 = 160.10$ pH. The dielectric permittivities of the effective media are $\epsilon_s = 0.76$ and $\epsilon_c = 9.13$. (b) From the outermost (I) to the central (IV) divisions of the meta-atom, each equivalent circuit branch or transmission line section is modeled based on a distinct geometric topology. The electrical lengths of transmission lines are approximately $\Theta_d = 35°$, $\Theta_s = 9°$, and $\Theta_c = 109°$ when referenced at 30 GHz.

$r_o = 1.72$ mm, $r_i = 0.42$ mm, $a = 1.7$ mm, $b_1 = 1.6$ mm, $b_2 = 1.2$ mm, $h_r = 1.7$ mm, $h_f = 2.2$ mm, and $h_p = 3.4$ mm.

The equivalent circuit–transmission line model is presented in Fig. 8, where a lumped capacitor C_3 is added to each of the circuit branch II on the symmetrical sides, which are then bridged by a lumped inductor L_3. The central loading more explicitly divides the effective dielectric medium into sandwiched transmission line sections, as indicated in Fig. 8(a). The full-wave simulated and circuit-calculated S-parameters, respectively, for the revised 3-D meta-atom and the equivalent circuit–transmission line model are compared in Fig. 9. The transmission and reflection coefficients obtained from circuit calculations closely match the results from full-wave simulations throughout the ultrawide operating frequency range, with subtle differences in out-of-band rejections which are visually exaggerated by the dB scale. While largely retaining

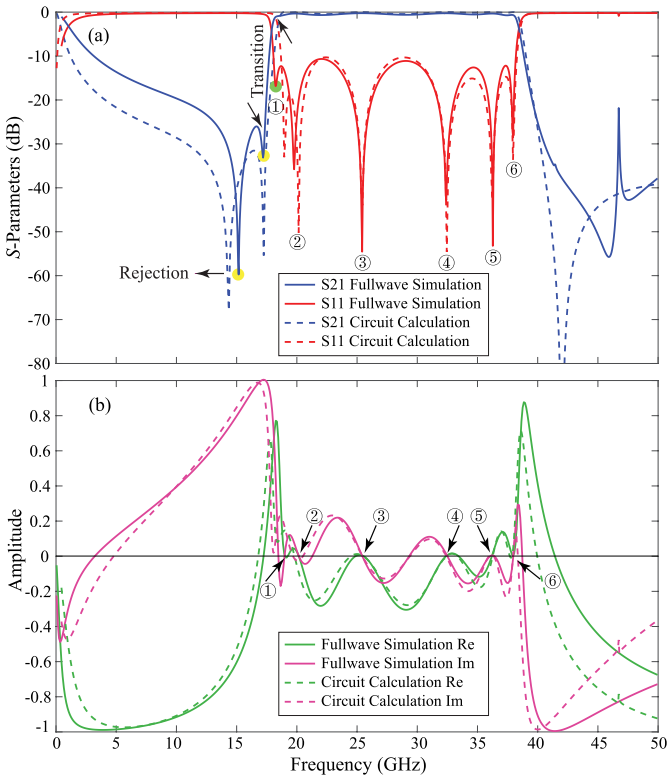

Fig. 9. Full-wave simulated and circuit-calculated transmission and reflection coefficients for the revised ultrawide FSS. (a) S-parameters in the dB scale. (b) Real and imaginary parts of the reflection coefficients.

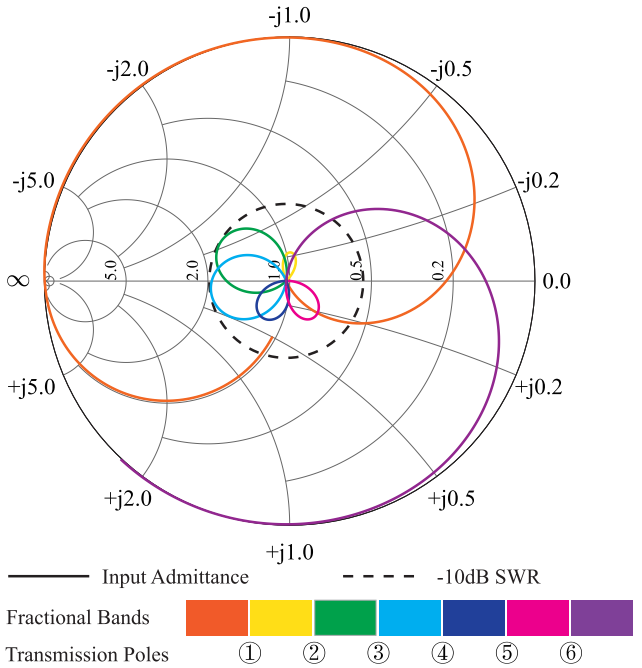

Fig. 10. Admittance Smith Chart for the revised 3-D meta-atom. The five knot-like loops correspond to the fractional bands in-between the six transmission poles. The rapid approach to and departure from the center of the locus indicates steep roll-off skirts at both the lowest and highest operating frequencies.

the conclusions from Fig. 5, the positions of the newly introduced pole and zeros are dominated by the periodicity p and gap g, corresponding to the equivalent lumped elements C_3 and L_3. In contrast to Fig. 3, the fractional bandwidth remains almost unchanged while the low-frequency roll-off has steepened to approximately 20 dB/GHz followed by a broad rejection band, due to the creation of one transmission pole and two transmission zeros on the far left of the passband. By introducing the new geometric features as a whole, the passband spans from 18.2 to 38.3 GHz, aiming for a 10 dB level of return loss. Therefore, bilateral sharp transitions and wide out-of-band rejections are achieved at the cost of only a 1.5% reduction in relative bandwidth. The reliability of this design approach is verified by cross-checking the HFSS simulated and the ADS calculated real and imaginary parts of the reflection coefficients as exhibited in Fig. 9(b).

As illustrated in Fig. 10, the Smith Chart intuitively justifies the bilateral sharp transitions and broad bandwidth. In such an ultrawide operating frequency range, the introduction of a new geometry (i.e., slits) inevitably leads to unpredictable degradation of the already optimized in-band S-parameters. By reconfiguring transmission line sections and circuit components with the aid of the Smith Chart, it becomes more efficient to incorporate compensatory structures (i.e., central loading) and reoptimize the dimensional parameters. As detailed in Section IV, this finalized ultrawide bandpass filter has been 3-D-printed and experimentally validated for transmission and reflection coefficients under normal and oblique angles for both TE and TM modes.

B. Dual-Band Bandpass FSS With Near-Equal Bandwidth

The versatility and potential of the proposed centrally loaded 3-D prototype in bandpass filtering can be further revealed by strategically introducing a transmission zero at the center of the ultrawide passband, effectively dividing it into two nearly equal bands. Dual-band bandpass filters are indispensable across a range of telecommunication applications, such as distributing different data streams in wireless communications, differentiating uplink and downlink in satellite systems, and segregating specific frequencies for various medical imaging modules [30], [31], [32], [33]. The authors primarily aim to develop near-equal passbands on the basis of the 3-D meta-atom prototyped in Section II, instead of introducing multiple transmission zeros (i.e., incorporating geometric features), which leads to complex EM couplings and thereby deteriorating the overall frequency response. The incremental benefit of an extremely sharp transition on the left side of the lower passband is beyond the scope of this section, especially due to space constraints. As shown in Fig. 11(a), and in comparison to Fig. 1, the original side enclosures (blue) are significantly stretched along the transmission path while slimmed in the other direction. Additional rectangular plates (orange) are again integrated to vertically enclose the center, ensuring the stability of transmission and reflection coefficients throughout the K–Ka spectra. The dimensional parameters, as also referenced in Fig. 2, are reconfigured for optimized frequency response, where $w_1 = 150\ \mu m$, $w_2 = 75\ \mu m$, $p = 2.9$ mm, $d = 1.7$ mm, $s = 0.175$ mm, $r_o = 1.7$ mm, $r_i = 0.6$ mm, $a = 1.7$ mm, $b_1 = 0.9$ mm, $b_2 = 2.4$ mm, $h_r = 1.7$ mm, $h_f = 2.2$ mm, and $h_p = 3.4$ mm.

The equivalent circuit–transmission line model has been accordingly revised to reflect the rescaled patch enclosures

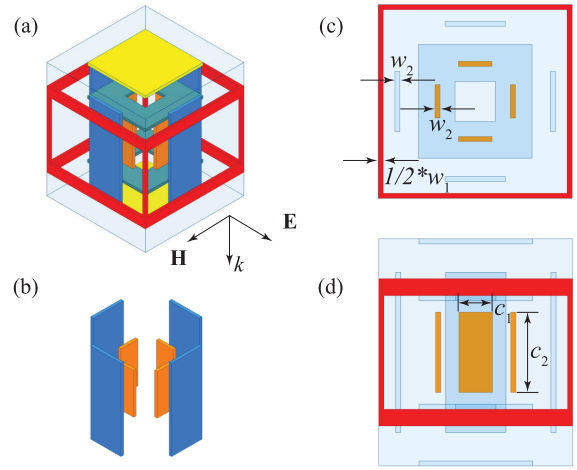

Fig. 11. Revised 3-D meta-atom for dual-band bandpass filtering with near-equal bandwidth. (a) Assembled unit-cell geometry. (b) Relative position of the added central loading (in orange). (c) and (d) Top and side views where $c_1 = 0.5$ mm and $c_2 = 1.2$ mm.

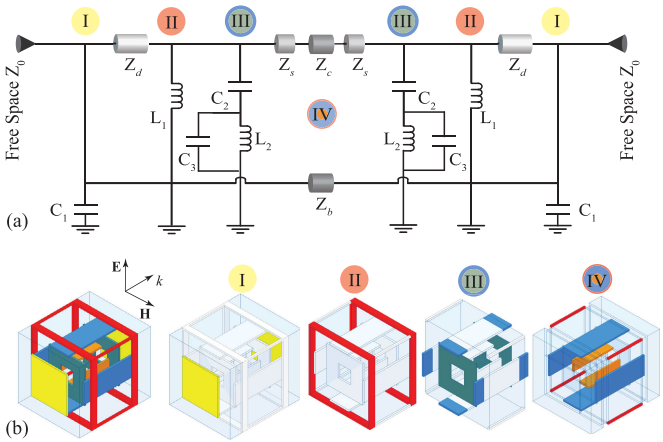

Fig. 12. Equivalent circuit–transmission line modeling for the dual-band 3-D meta-atom. (a) Lumped circuit elements $C_1 = 12.95$ fF, $C_2 = 18.71$ fF, $C_3 = 16.83$ fF, $L_1 = 939.44$ pH, and $L_2 = 867.74$ pH. The dielectric permittivities of the effective media are $\epsilon_s = 1.28$, $\epsilon_c = 0.24$, and $\epsilon_b = 0.37$. (b) From the outermost (I) to the central (IV) divisions of the meta-atom. The electrical lengths of transmission lines are approximately $\Theta_d = 29°$, $\Theta_s = 27°$, $\Theta_c = 114°$, and $\Theta_b = 92°$ when referenced at 30 GHz.

and newly incorporated central loading along the EM wave propagation direction, as presented in Fig. 12, where a lumped capacitor C_3 is added to each of the circuit branches III and a transmission line section Z_b bridges the circuit branches I on the symmetrical sides. Segmented transmission lines are still adopted to represent variations in the effective media dictated by the central waveguiding structure. The full-wave simulated and circuit-calculated transmission and reflection coefficients align closely across a broad frequency range up to 50 GHz, as shown in Fig. 13(a). In contrast to Fig. 3, besides the central transmission zero, another one introduced to the right of the operating spectrum has further contributed to the upper out-of-band rejection. The reliability and accuracy of the equivalent circuit–transmission line modeling can be reconfirmed by comparing the real and imaginary parts (i.e., equivalently magnitude and phase) of the reflection coefficients obtained from full-wave simulation and circuit calculation, as exhibited in Fig. 13(b).

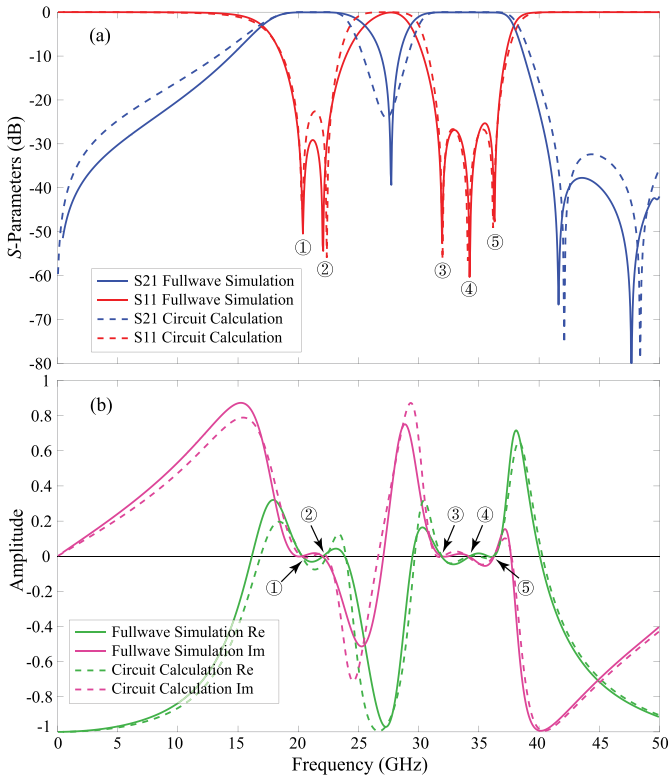

Fig. 13. Full-wave simulated and circuit-calculated transmission and reflection coefficients for the dual-band FSS. (a) S-parameters in the dB scale. (b) Real and imaginary parts of the reflection coefficients.

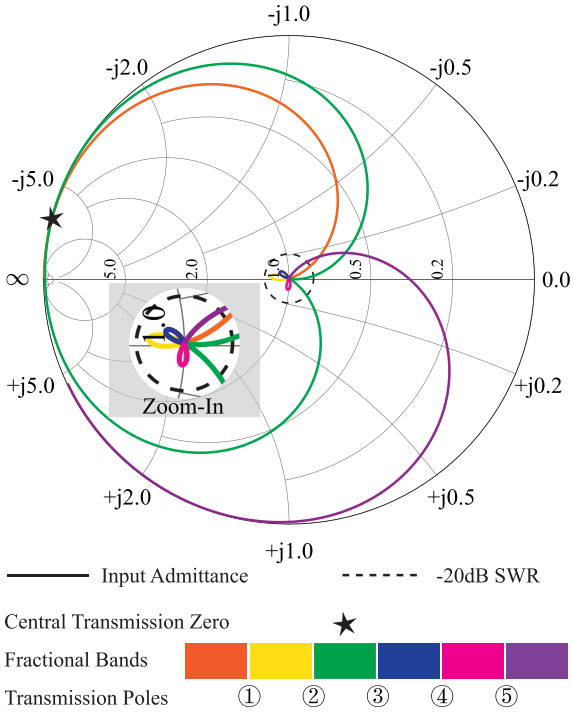

Fig. 14. Admittance Smith Chart for the dual-band 3-D meta-atom. The yellow knot-like loop corresponds to the fractional band in-between the first two transmission poles, while the blue and magenta ones correspond to the fractional bands in-between the last three transmission poles. The locus from the second to third transmission poles is tangential to the Smith Chart at the central transmission zero.

As illustrated in Fig. 14, the Smith Chart intuitively indicates all transmission poles and demonstrates how the introduction of a central transmission zero splits the broad

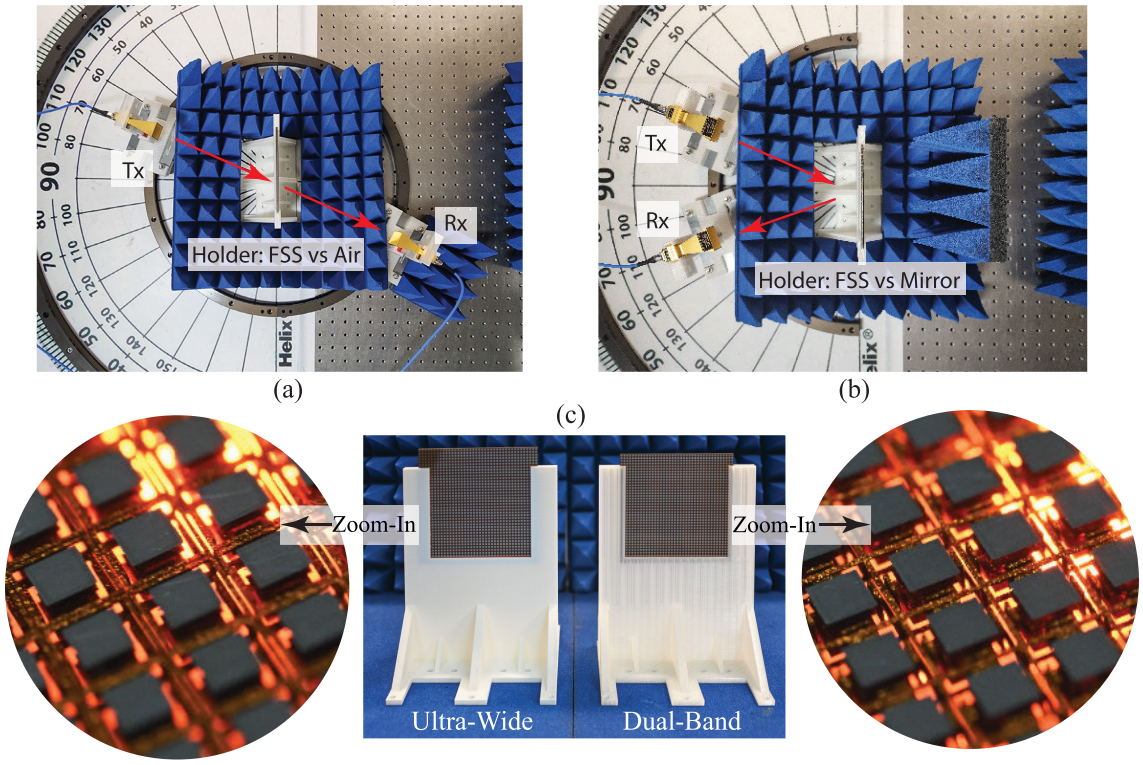

Fig. 15. Experimental setups and fabricated samples. (a) and (b) Top views of transmission and reflection measurements at an oblique incidence (e.g., 20°) for the TM and TE modes, respectively. (c) Fabricated ultrawide and dual-band FSSs (40 × 40 unit cells) framed in holders, with respective dimensions of 124 × 124 × 3.4 mm and 116 × 116 × 3.4 mm. The zoomed-in view photos are taken with a 50 mm 1:1 macro lens at a specific inclination, illuminated by torchlight.

operating spectrum into two near-equal passbands. In contrast to the admittance loci of the ultrawide bandpass filters as shown in Figs. 6 and 10, which consecutively pass-through the center of the Smith Chart and wind within the −10-dB SWR circle, the locus of the dual-band design rapidly diverges from the center after crossing it twice, tangentially touches the rim of the Smith Chart, and then crosses the center for three more times in quick succession. By adjusting the tangent point, the frequency corresponding to the transmission zero can be relocated. The in-band reflection coefficients have been suppressed to −20 dB, consequently, the knot-like loops are significantly miniaturized. This dual-band bandpass filter has also been fabricated utilizing multimaterial additive manufacturing techniques, with its frequency response verified through comprehensive measurements in Section IV.

IV. Experimental Setups and Measurements

The transmission and reflection paths, as displayed in Fig. 15(a) and (b), consist of a vector network analyzer (VNA), coaxial cables, paired K- and Ka-band horn antennas, slide rails and carriers, and 3-D-printed polymer holders for antennas and samples. The aperture sizes of the high-gain horn antennas used in the experimental validation are 23.1 × 30.7 mm for the K-band and 21.9 × 27.4 mm for the Ka-band, which are approximately 5% of the fabricated FSS sample sizes, making the truncation effect insignificant. The floating bench is surrounded by flat and pyramidal foam absorbers to minimize interference. The transmissivity and reflectivity of the FSSs are, respectively, referenced to free space and metallic plates, which correspond to near-perfect transmission and reflection at the FSS location. Transmissivity is determined by the ratio of the absolute power transmitted with and without the FSS sample, while reflectivity is calculated from the ratio of the absolute power reflected with the FSS sample and with a metallic mirror of the same size.

The DragonFly 3-D printer is equipped with dual printing heads to simultaneously print silver nanoparticle conductive ink and acrylate dielectric ink, cured by infrared (IR) and ultraviolet (UV) light. Key specifications include a minimum linewidth of 75 μm, a minimum gap of 100 μm, a resolution of 18 μm in the orthogonal horizontal directions and 10 μm in the vertical direction, a minimum conductive layer thickness of 1.18 μm, and a minimum dielectric layer thickness of 10 μm, with tolerances maintained within 40 μm in the horizontal directions. The inks are meticulously deposited onto the Kapton surface using a layer-by-layer process. After each layer solidifies, successive layers are applied, progressively constructing the desired structure. Subwavelength geometries can be recognized from the zoomed-in view pictures in Fig. 15(c), including the hexahedral grid with or without gaps, square patches, square rings, and vertical enclosures.

In practice, the acrylate ink used for fabricating FSSs exhibits dielectric attenuation (i.e., $\tan\delta = 0.012$). The measured transmission and reflection coefficients will be compared with simulations that incorporate such a loss tangent for experimental verification. With a physical insight into time–frequency-domain mutual conversions, external interference can be effectively reduced without distorting the raw data by implementing time-gating in postprocessing. In the absence of focusing lens assemblies, the reflected wave can be distin-

TABLE I
COMPARISON OF NOTABLE FABRICATED WIDEBAND BANDPASS FSS FILTERS

Ref	Polarization	Band	3dB FBW	Zeros		Poles	Angular Stability (deg)		Electrical Length (λ_L)	Central IL (dB)
				Left	Right	In-Band	TE Mode	TM Mode		
[34]	TE Only	S-C	130.4%	0	0	4	40	-	0.03 x 0.03 x 0.16	0.7
[25]	TE Only	C	21.4%	0	0	3	45	-	0.15 x 0.15 x 0.52	0.4
[22]	TE Only	C	78.7%	0	0	4	40	-	0.06 x 0.10 x 0.27	1.0
[35]	TE Only	C-Ku	78.5%	1	1	-	45	-	0.18 x 0.18 x 0.18	3.0
[38]	Both	S	13.4%	1	1	2	20	40	0.22 x 0.22 x 0.28	2.1
[27]	Both	S	26.3%	0	2	2	60	60	0.09 x 0.09 x 0.22	1.1
[24]	Both	C-X	22.9%	0	2	2	40	40	0.18 x 0.18 x 0.27	0.7
[36]	Both	X	30.8%	0	2	2	30	45	0.27 x 0.27 x 0.25	0.3
[26]	Both	Ku	15.2%	1	2	2	10	20	0.62 x 0.62 x 0.25	2.0
[37]	Both	K-Ka	28.6%	0	0	3	45	45	0.29 x 0.29 x 0.47	0.8
Proposed	Both	K-Ka	69.1%	2	1	6	45*	30*	0.19 x 0.19 x 0.21	1.6

* Approximately 40% 3dB fractional bandwidth can be achieved at 55° in TE mode and at 65° in TM mode, respectively.

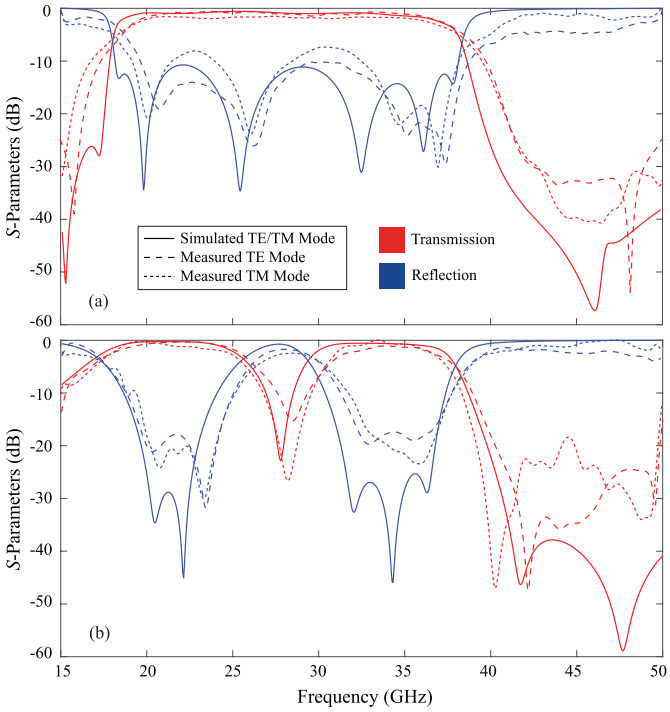

Fig. 16. Simulated and measured frequency responses under normal incidence for (a) ultrawide and (b) dual-band bandpass filters. Full-wave simulated transmission and reflection coefficients for the TE and TM modes cannot be distinguished from each other due to the symmetry of the proposed meta-atoms, while the measured results exhibit slight variations between the modes. Since the cutoff frequency of the K-band horn antennas is 15 GHz, the presented simulation and experimental curves start at 15 GHz.

guished from the internal noise using the transmission mode of a pair of horn antennas, as shown in Fig. 15(b). To approximate reflection under normal incidence, the antennas especially feature a small inclination (e.g., 5°), which nonetheless has a negligible effect on the frequency response. As shown in Fig. 16(a) and (b), the simulated and measured results for the ultrawide and dual-band FSS filters under normal incidence match closely, with slight differences attributed to fabrication tolerances, alignment imperfections, and minor sidelobes in the antenna's radiation pattern. However, the discrepancies on both sides of the passbands are at the −30-dB level (i.e., 0.1% of the power), which is considered acceptable for spatial filter measurements. The measured in-band insertion loss of our proposed designs is approximately 1.6 dB, which is slightly higher than the full-wave simulated results but still well below the 3-dB standard defined for operating bandwidth. The ultrawide bandpass filter covers a −3-dB bandwidth from 18.23 to 37.49 GHz, while the dual-band design offers two nearly equal absolute bandwidths, respectively, spanning 17.21–25.29 and 29.62–37.45 GHz. Although the proposed FSS filters are designed for scenarios with normally incident EM waves, their robustness under oblique incidence has also been tested through full-wave simulations and experimental validations. As demonstrated in Figs. 17 and 18, the operating frequency range of the ultrawideband FSS stays largely stable up to 45° for the TE mode and 30° for the TM mode, while the passbands of the dual-band FSS hold firm up to 50° for the TE mode and 30° for the TM mode, aiming to approach their performance under normal incidence. The frequency responses of these filters remain highly competitive even at higher angles compared to the existing designs in the literature. Specifically, the wideband FSS can achieve a narrower bandwidth of 41.5% at 55° for the TE mode and 42.1% at 65° for the TM mode, which is still broader than the tabulated polarization insensitive designs.

The experimentally verified state-of-the-art wideband bandpass FSSs have been tabulated in Table I [22], [24], [25], [26], [27], [34], [35], [36], [37], [38]. Polarization insensitivity is essential for spatial filters (e.g., FSS-based radar domes),

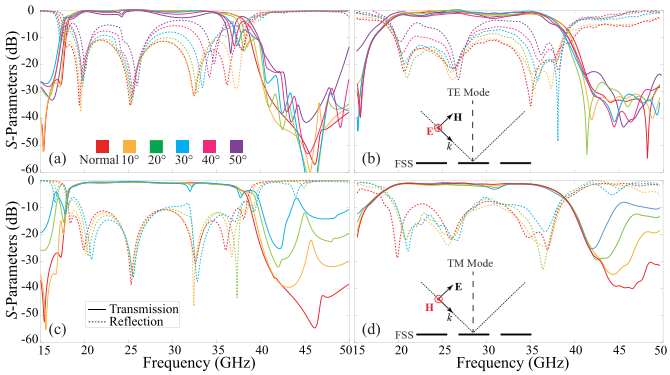

Fig. 17. Robustness tests for ultrawide bandpass FSS under oblique incidence. (a) Full-wave simulated TE mode. (b) Measured TE mode. (c) Full-wave simulated TM mode. (d) Measured TM mode.

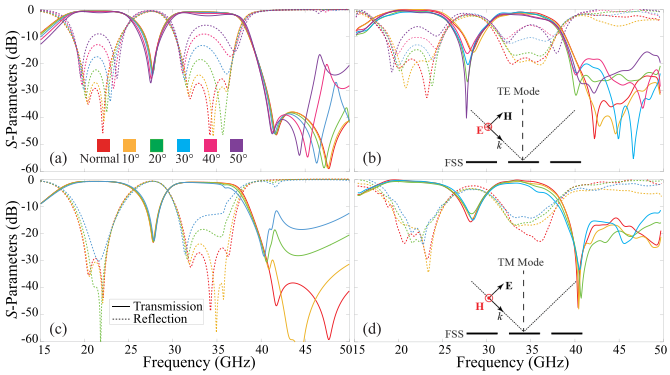

Fig. 18. Robustness tests for dual-band bandpass FSS under oblique incidence. (a) Full-wave simulated TE mode. (b) Measured TE mode. (c) Full-wave simulated TM mode. (d) Measured TM mode.

as the polarization of the incident wave is often unpredictable. Despite designs employing asymmetric unit-cell shapes that can achieve impressive performance with greater flexibility for a single polarization mode, their inherent polarization sensitivity imposes a limitation on their suitability for practical applications. It also becomes increasingly challenging to obtain broad bandwidth at a higher frequency spectrum because of the hiked material attenuation, therefore a fair comparison is drawn starting from the C-band onward. Most fully optimized FSS designs feature wide out-of-band rejection on the higher side of the operating frequency range, whereas additional transmission zeros on the lower side are desirable but require a tradeoff in bandwidth. Our proposed ultrawideband FSS, despite operating across the K–Ka spectra, still exhibits low insertion loss in the central frequency range. Featuring six transmission poles, its passband bandwidth is more than double that of the other tabulated designs. The transmission coefficient curve uniquely includes two low-frequency transmission zeros, ensuring an extensive low-frequency attenuation region. Due to the inherent integration properties of the 3-D meta-atom, the proposed design is also the thinnest relative to the wavelength of the lowest operating frequency λ_L. Despite the lack of standardized and unambiguous evaluation criteria for the limited number of existing multiband bandpass FSSs, our proposed dual-band FSS excels in the absolute bandwidth, in-band transmission, and insertion loss for each passband [30], [39], [40], [41].

V. Conclusion

Facilitated by advanced multimaterial additive manufacturing techniques, the frequency-selective potential of the meta-atom lattice can be thoroughly exploited by lifting the inherent constrains in topological optimization of conventional layered 2-D-FSSs or quasi-3-D FSSs that adopt vias or microstrip line insertions. The proposed 3-D prototype draws inspiration from the centrally loaded double-layer FSS with bandpass filtering performance. By freely assembling fundamental geometries within a 3-D meta-atom lattice, multiple transmission poles are introduced without substantially increasing the computational cost of analysis and synthesis. The authors present a generalized approach for constructing equivalent circuit–transmission line models, the frequency responses of which align accurately with the full-wave simulations of an evolutionary series of 3-D meta-atoms. Combined with the real-time tuning function in the ADS, Fig. 5 provides a qualitative design aid that effectively bridges the gaps in-between dimensional parameters and material attributes, circuit elements and transmission line properties, and frequency responses. These design tools are applicable to optimize a variety of FSS-based structures for desirable features such as wide bandwidth, efficient in-band transmissions, steep roll-off skirts, and clear out-of-band rejections. Upon request, closed-form expressions relating the equivalent circuit components to the geometric dimensions of the meta-atom can be derived using the fast semi-analytical design method [9]. On the basis of the proposed 3-D prototype, by isolating grid frames or stretching the vertical patch enclosures, additional transmission zeros are strategically inserted at distinct positions on the operating frequency spectrum to, respectively, obtain bilateral sharp transitions and specified passband divisions, which are highly sought-after in the realm of spatial filters.

Particularly configured for the application-driven K–Ka spectra, the ultrawide FSS spans a −3-dB passband from 18.23 to 37.49 GHz, while the dual-band FSS offers a pair of near-equal absolute passbands ranging from 17.21 to 25.29 and 29.62 to 37.45 GHz. Both filters are inherently polarization insensitive due to the symmetric geometries of their meta-atoms whose robustness against oblique incident EM waves has also been experimentally verified for both TE and TM modes. The filter response order can be further enhanced by evolving the simple FSS shapes through the incorporation of additional geometric features, while the operating frequency can be extended up-to the D-band through rescaling without exceeding fabrication capabilities or material loss limitations. At the cost of increased geometric complexity in the meta-atom structure, multiple in-band transmission zeros can be realized. However, to mitigate the side effects of more complex mutual couplings, the difficulty in topological optimization may also increase accordingly. Similar to the demonstrated evolutionary process, a highly selective narrowband 3-D FSS may be developed based on the 2-D FP FSS, thereby underscoring the substantial potential of 3-D meta-atoms from a more comprehensive perspective. The proposed 3-D meta-atoms not only exhibit compelling frequency-selective properties but also establish a promising

foundation for advancing applications in metamaterials and array-based structures.

ACKNOWLEDGMENT

The authors sincerely appreciate the excellent support and contribution in fabrication provided by Mr. Bobby Chan and Mr. Tomer Dahan, as well as the dedicated Research and Development teams at Nano Dimension.

REFERENCES

[1] X. Lv, Z. Luo, and Y. Yang, "3-D centrally-loaded FSS leveraging conductive and dielectric multimaterial additive manufacturing for broadband performance," in *IEEE MTT-S Int. Microw. Symp. Dig.*, Jun. 2024, pp. 18–21.

[2] B. A. Munk, *Frequency Selective Surfaces: Theory and Design*. Hoboken, NJ, USA: Wiley, 2000.

[3] R. Mittra, C. H. Chan, and T. Cwik, "Techniques for analyzing frequency selective surfaces—A review," *Proc. IEEE*, vol. 76, no. 12, pp. 1593–1615, Dec. 1988.

[4] C. L. Holloway, E. F. Kuester, J. A. Gordon, J. O'Hara, J. Booth, and D. R. Smith, "An overview of the theory and applications of metasurfaces: The two-dimensional equivalents of metamaterials," *IEEE Antennas Propag. Mag.*, vol. 54, no. 2, pp. 10–35, Apr. 2012.

[5] H. Chen, X. Hou, and L. Deng, "Design of frequency-selective surfaces radome for a planar slotted waveguide antenna," *IEEE Antennas Wireless Propag. Lett.*, vol. 8, pp. 1231–1233, 2009.

[6] N. Liu, X. Sheng, C. Zhang, and D. Guo, "Design of frequency selective surface structure with high angular stability for radome application," *IEEE Antennas Wireless Propag. Lett.*, vol. 17, no. 1, pp. 138–141, Jan. 2018.

[7] F. Costa and A. Monorchio, "A frequency selective radome with wideband absorbing properties," *IEEE Trans. Antennas Propag.*, vol. 60, no. 6, pp. 2740–2747, Jun. 2012.

[8] X. Lv, W. Withayachumnankul, and C. Fumeaux, "Single-FSS-Layer absorber with improved bandwidth–thickness tradeoff adopting impedance-matching superstrate," *IEEE Antennas Wireless Propag. Lett.*, vol. 18, pp. 916–920, 2019.

[9] X. Lv, S. Chen, A. Galehdar, W. Withayachumnankul, and C. Fumeaux, "Fast semi-analytical design for single-FSS-layer circuit-analog absorbers," *IEEE Open J. Antennas Propag.*, vol. 1, pp. 483–492, 2020.

[10] B. A. Munk, P. Munk, and J. Pryor, "On designing Jaumann and circuit analog absorbers (CA Absorbers) for oblique angle of incidence," *IEEE Trans. Antennas Propag.*, vol. 55, no. 1, pp. 186–193, Jan. 2007.

[11] O. Luukkonen, F. Costa, C. R. Simovski, A. Monorchio, and S. A. Tretyakov, "A thin electromagnetic absorber for wide incidence angles and both polarizations," *IEEE Trans. Antennas Propag.*, vol. 57, no. 10, pp. 3119–3125, Oct. 2009.

[12] J. Lai, X. Lv, and Y. Yang, "A 3-D printed 140 GHz multifocal dielectric transmitarray antenna for 2-D mechanical beam scanning," *IEEE Antennas Wireless Propag. Lett.*, vol. 23, pp. 1366–1370, 2024.

[13] A. H. Abdelrahman, A. Z. Elsherbeni, and F. Yang, "Transmission phase limit of multilayer frequency-selective surfaces for transmitarray designs," *IEEE Trans. Antennas Propag.*, vol. 62, no. 2, pp. 690–697, Feb. 2014.

[14] J. R. Reis, M. Vala, and R. F. S. Caldeirinha, "Review paper on transmitarray antennas," *IEEE Access*, vol. 7, pp. 94171–94188, 2019.

[15] J. Wang et al., "Metantenna: When metasurface meets antenna again," *IEEE Trans. Antennas Propag.*, vol. 68, no. 3, pp. 1332–1347, Mar. 2020.

[16] Y. Dong and T. Itoh, "Metamaterial-based antennas," *Proc. IEEE*, vol. 100, no. 7, pp. 2271–2285, Jul. 2012.

[17] N. Wang, Q. Liu, C. Wu, L. Talbi, Q. Zeng, and J. Xu, "Wideband Fabry–Perot resonator antenna with two complementary FSS layers," *IEEE Trans. Antennas Propag.*, vol. 62, no. 5, pp. 2463–2471, May 2014.

[18] H. Attia, M. L. Abdelghani, and T. A. Denidni, "Wideband and high-gain millimeter-wave antenna based on FSS Fabry–Perot cavity," *IEEE Trans. Antennas Propag.*, vol. 65, no. 10, pp. 5589–5594, Oct. 2017.

[19] Y.-M. Yu, C.-N. Chiu, Y.-P. Chiou, and T.-L. Wu, "A novel 2.5-dimensional ultraminiaturized-element frequency selective surface," *IEEE Trans. Antennas Propag.*, vol. 62, no. 7, pp. 3657–3663, Jul. 2014.

[20] T. Hussain, Q. Cao, J. K. Kayani, and I. Majid, "Miniaturization of frequency selective surfaces using 2.5-D knitted structures: Design and synthesis," *IEEE Trans. Antennas Propag.*, vol. 65, no. 5, pp. 2405–2412, May 2017.

[21] H. Lin et al., "Filtenna-filter-filtenna-based FSS with simultaneous wide passband and wide out-of-band rejection using multiple-mode resonators," *IEEE Trans. Antennas Propag.*, vol. 71, no. 6, pp. 5046–5056, Jun. 2023.

[22] H. Li, B. Li, and L. Zhu, "A generalized synthesis technique for high-order and wideband 3-D frequency-selective structures with Chebyshev functions," *IEEE Trans. Antennas Propag.*, vol. 69, no. 7, pp. 3936–3944, Jul. 2021.

[23] H. Li, B. Li, and L. Zhu, "Wideband bandpass frequency-selective structures on stacked slotline resonators: Proposal and synthetic design," *IEEE Trans. Antennas Propag.*, vol. 68, no. 10, pp. 7068–7078, Oct. 2020.

[24] B. Li and Z. Shen, "Three-dimensional dual-polarized frequency selective structure with wide out-of-band rejection," *IEEE Trans. Antennas Propag.*, vol. 62, no. 1, pp. 130–137, Jan. 2014.

[25] W. Zhang, L. Zhu, and B. Li, "Synthesis design of inductively-coupled 3-D bandpass frequency-selective structures based on equivalent SOL-extracted circuit model," *IEEE Trans. Antennas Propag.*, vol. 70, no. 12, pp. 11881–11891, Dec. 2022.

[26] Z. Zhao et al., "Bandpass FSS with zeros adjustable quasi-elliptic response," *IEEE Antennas Wireless Propag. Lett.*, vol. 18, pp. 1184–1188, 2019.

[27] J. Zhu, W. Gao, Y. Shi, W. Li, and W. Tang, "A dual-polarized bandpass frequency selective surface with stable response," *IEEE Antennas Wireless Propag. Lett.*, vol. 20, no. 5, pp. 673–677, May 2021.

[28] M. Li, Y. Yang, Y. Zhang, and F. Iacopi, "3-D printed vertically integrated composite right/left-handed transmission line and its applications to microwave circuits," *IEEE Trans. Microw. Theory Techn.*, vol. 72, no. 6, pp. 3311–3321, Jun. 2024.

[29] J. Zhu, M. Li, J. Lai, and Y. Yang, "Multimaterial additively manufactured transmissive spin-decoupled polarization-maintaining metasurfaces," *Laser Photon. Rev.*, vol. 17, no. 12, Dec. 2023, Art. no. 2300433.

[30] Y. Li, Z. Zhao, Z. Tang, and Y. Yin, "Differentially fed, dual-band dual-polarized filtering antenna with high selectivity for 5G sub-6 GHz base station applications," *IEEE Trans. Antennas Propag.*, vol. 68, no. 4, pp. 3231–3236, Apr. 2020.

[31] U. Naeem, S. Bila, M. Thévenot, T. Monédière, and S. Verdeyme, "A dual-band bandpass filter with widely separated passbands," *IEEE Trans. Microw. Theory Techn.*, vol. 62, no. 3, pp. 450–456, Mar. 2014.

[32] R. Deng, F. Yang, S. Xu, and M. Li, "An FSS-backed 20/30-GHz dual-band circularly polarized reflectarray with suppressed mutual coupling and enhanced performance," *IEEE Trans. Antennas Propag.*, vol. 65, no. 2, pp. 926–931, Feb. 2017.

[33] A. Balaji, R. Krishnan, S. Vanaja, T. Sowmiya, and R. Vanitha, "Design and analysis of tri-band stop FSS for medical instruments shielding application," in *Proc. 6th Int. Conf. Commun. Electron. Syst. (ICCES)*, Jul. 2021, pp. 1–5.

[34] Y. Ma, X. Zhang, S. Wu, Y. Yuan, and N. Yuan, "A hybrid 2D–3D miniaturized multiorder wide bandpass FSS," *IEEE Antennas Wireless Propag. Lett.*, vol. 21, pp. 307–311, 2022.

[35] P. Wang, W. Jiang, T. Hong, Y. Li, G. F. Pedersen, and M. Shen, "A 3-D wide passband frequency selective surface with sharp roll-off sidebands and angular stability," *IEEE Antennas Wireless Propag. Lett.*, vol. 21, no. 2, pp. 252–256, Feb. 2022.

[36] A. Lalbakhsh, M. U. Afzal, K. P. Esselle, and S. L. Smith, "All-metal wideband frequency-selective surface bandpass filter for TE and TM polarizations," *IEEE Trans. Antennas Propag.*, vol. 70, no. 4, pp. 2790–2800, Apr. 2022.

[37] W. Y. Yong and A. A. Glazunov, "Miniaturization of a fully metallic bandpass frequency selective surface for millimeter-wave band applications," *IEEE Trans. Electromagn. Compat.*, vol. 65, no. 4, pp. 1072–1080, Apr. 2023.

[38] J. Zhu, W. Tang, C. Wang, C. Huang, and Y. Shi, "Dual-polarized bandpass frequency-selective surface with quasi-elliptic response based on square coaxial waveguide," *IEEE Trans. Antennas Propag.*, vol. 66, no. 3, pp. 1331–1339, Mar. 2018.

[39] M. Yan et al., "A quad-band frequency selective surface with highly selective characteristics," *IEEE Microw. Wireless Compon. Lett.*, vol. 26, no. 8, pp. 562–564, Aug. 2016.

[40] H. Zhou et al., "A triband second-order frequency selective surface," *IEEE Antennas Wireless Propag. Lett.*, vol. 10, pp. 507–509, 2011.

[41] B. Rahmati and H. R. Hassani, "Multiband metallic frequency selective surface with wide range of band ratio," *IEEE Trans. Antennas Propag.*, vol. 63, no. 8, pp. 3747–3753, Aug. 2015.

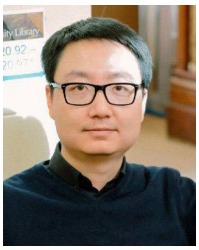

Xiaojing Lv (Member, IEEE) received the Ph.D. degree in electrical and electronic engineering from The University of Adelaide, Adelaide, SA, Australia, in 2021.

He is currently a Post-Doctoral Research Fellow with the Wireless Communication and Networking Laboratory, and a Lecturer with the School of Electrical and Data Engineering, University of Technology Sydney, Ultimo, NSW, Australia. His research interests include computational electromagnetics, advanced metamaterial structures, frequency-selective surface filters, antenna arrays, CubeSat antennas, and multimaterial additive manufacturing.

Dr. Lv was awarded the Australian Government's Research Training Program Scholarship from 2017 to 2021 and First Place in the Early Career Paper Competition at the IEEE MTT-S International Microwave Symposium (IMS) in 2024.

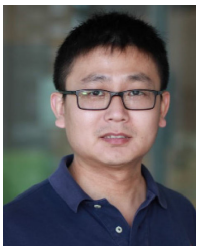

Yang Yang (Senior Member, IEEE) was born in Bayannur, Inner Mongolia, China. He received the Ph.D. degree in electronic engineering from the Department of Electrical and Computer Systems Engineering, Monash University, Clayton, VIC, Australia, in 2013.

In 2012, he joined Rain Bird Australia, Melbourne, VIC, serving as an Asia Pacific GSP Engineer. In April 2015, he returned to academia, holding the position of Senior Research Associate in microwave and antenna technologies at Macquarie University, Sydney, NSW, Australia. In April 2016, he was appointed as a Research Fellow with the State Key Laboratory of Terahertz and Millimeter Waves, City University of Hong Kong, Hong Kong. In December 2016, he was appointed as a Scholarly Teaching Fellow at the University of Technology Sydney (UTS), Ultimo, NSW. He is currently an Associate Professor and a Group Leader of 3-D Millimeter-Wave and Terahertz Circuits and Antennas at UTS Tech Laboratory, Botany, NSW. He has over 260 international publications in microwave, millimeter-wave, and terahertz circuits and antennas. His research interests include millimeter-wave and subterahertz technologies in 5G and beyond and biomedical applications.

Dr. Yang is a Committee Member of IEEE MTT-S TC-28 Biological Effects and Medical Applications, the AP-S Technical Committee on Antenna Measurements, and the AP-S Technical Directions Committee. He was selected as one of the "Top 2% Most Highly Cited Scientists by Stanford" every year in 2019. He is the Inaugural Chair of IEEE MTT-S TC-17 Microwave Materials and Processing Technologies. His appointments at IEEE NSW Section, Region 10, include being the Committee Member of the IEEE NSW Section, the Treasurer from 2018 to 2019, and the Chair/Vice Chair of the IEEE NSW AP/MTT Joint Chapter from 2020 to 2024, the Secretary of IEEE NSW PH/ED/SSC/CAS Joint Chapter in 2019, the Inaugural Committee/Treasurer in 2020, and Vice Chair of IEEE NSW Electron Devices Chapter from 2022 to 2024. He also volunteered in various conference organizing committees, such as the General Co-Chair of the 2025 Australian Microwave Symposium. He is an Associate Editor of IEEE ACCESS from 2018 to 2022, IEEE TRANSACTIONS ON MICROWAVE THEORY AND TECHNIQUES in October 2022, and IEEE MICROWAVE AND WIRELESS TECHNOLOGY LETTERS in October 2024, a Guest Editor of IEEE ANTENNAS AND WIRELESS PROPAGATION LETTERS in 2022 and PROCEEDINGS OF THE IEEE in 2024, and an Area Editor of *Microwave and Optical Technology Letters* from 2019 to 2024.

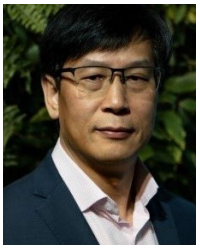

Zhen Luo received the Ph.D. degree in mechanical engineering from the National Engineering Research Center for CAD, Huazhong University of Science and Technology, Wuhan, China, in 2005.

He has held academic positions at prominent institutions including Shanghai JiaoTong University, Shanghai, China, Chinese University of Hong Kong, Hong Kong, The University of Sydney, Sydney, NSW, Australia, University of New South Wales, Sydney, and University of Technology Sydney (UTS), Ultimo, NSW. He has been an Associate Professor with the School of Mechanical Engineering, UTS, since 2017, where he leads the Advanced Metacomposite Materials and Structures (AMMS) Research Group. His interdisciplinary work focuses on advanced engineering materials and structures, particularly in aerospace and space engineering. He is an internationally recognized research scientist in computational materials design. His multidisciplinary research leverages electromagnetic, elastic, acoustic, and thermal energy absorption materials and structures, integrating numerical simulation, topology optimization, and additive manufacturing. He has published 252 peer-reviewed research articles, including 151 articles published in JCR Q1 journals, attracting over 8300 citations with an H-index of 53 (Google Scholar). He has secured six million in research funding, including five ARC Discovery Projects (Australian Research Council), and has successfully engaged with government and industry stakeholders.

Dr. Luo was selected as a Fellow of the International Association of Advanced Materials (IAAM) in 2023, and a member of several esteemed professional societies, including the International Association of Computational Mechanics (IACM), the International Society for Structural and Multidisciplinary Optimization (ISSMO), and the American Society of Mechanical Engineers (ASME). His accolades, including the World's Top 2% Research Scientists (Stanford University, since 2019), the ScholarGPS Highly Ranked Scholar (Top 0.05% Scholars Worldwide, #6 Topology Optimization, and #84 Mathematical Optimization) from 2017 to 2022, and the IAAM Scientist Award in 2020, as well as his recent appointments to the ARC Selection Advisory Committee (NIDG) from 2024 to 2026, underscore his international reputation, impact, and leadership in research. He is also Co-Chair of the 6th International Conference on Materials Science and Manufacturing Engineering (MSME) in 2025 and General Chair of the 1st International Conference on Design and Manufacturing in Advanced Materials and Structures (DMAMS) in 2025. He holds several editorial roles in international journals, such as Structural Multidisciplinary Optimization (JCR Q1), Frontiers in Bioengineering and Biotechnology–Biomechanics (JCR Q1), and Applied Sciences (JCR Q1).

J. Scott Tyo (Fellow, IEEE) received the Ph.D. degree in electrical engineering from the University of Pennsylvania, Philadelphia, PA, USA, in 1997.

He is currently the Head of the Electrical and Computer Systems Engineering Department, Monash University, Clayton, VIC, Australia, and he will become the Chief of the Platforms Division for the Defense Science and Technology Group, Canberra, ACT, Australia, beginning in 2025. Before joining Monash in 2022, he was the Head of the School of Engineering and Information Technology for UNSW Canberra at the Australian Defence Force Academy, Canberra, ACT, from 2015 to 2021, a Professor with the College of Optical Sciences, The University of Arizona, Tucson, AZ, USA, and an Associate Professor at the University of New Mexico, Albuquerque, NM, USA. His research interests include applied electromagnetics and optics.

Dr. Tyo is a Fellow of SPIE and Optica. He was a member of AdCom of the IEEE Antennas and Propagation Society and the Board of Directors of SPIE.